CRYSTAL GROWTH & DESIGN

pubs.acs.org/crystal

Article

# Bulky Phenylalkyl Substitutions to Bisthienoisatins and Thienoisoindigos

Dongho Yoo,* Akihiro Kohara, Minoru Ashizawa,* Tadashi Kawamoto, Hiroyasu Masunaga, Noboru Ohta, Hidetoshi Matsumoto, and Takehiko Mori*

Cite This: https://dx.doi.org/10.1021/acs.cgd.0c00087

Read Online

ACCESS | Metrics & More | Article Recommendations | Supporting Information

Downloaded via BIU SANTE on April 18, 2020 at 04:43:57 (UTC).
See https://pubs.acs.org/sharingguidelines for options on how to legitimately share published articles.

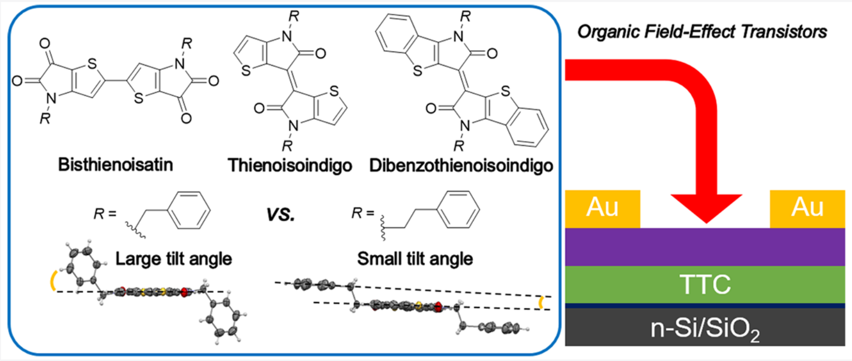

**ABSTRACT:** In order to investigate the effects of bulky substituents on the crystal structures and packing modes, *N*-benzyl (Bn) and *N*-2-phenylethyl (EtPh) substituents are introduced in bisthienoisatin (**BTI**), thienoisoindigo (**TIIG**), and dibenzothienoisoindigo (**DBTII**). These molecules maintain uniform stacking structures, though **EtPh-BTI** has a two-dimensional slipped-herringbone structure. The benzyl groups are largely distorted from the molecular core, and thin films of **Bn-TIIG** and **Bn-DBTII** show poor quality due to the two kinds of molecular orientations. In contrast, the 2-phenylethyl-substituted molecules enable suitable molecular packing owing to the ethylene spacer and show relatively good thin-film qualities as well as much improved transistor properties. The **BTI** derivatives show only electron transport, but other compounds exhibit ambipolar transistor properties. In particular, **EtPh-TIIG** and **EtPh-DBTII** show maximum hole mobilities of about 0.04−0.05 cm$^2$ V$^{-1}$ s$^{-1}$ together with moderate electron mobilities.

## INTRODUCTION

The development of organic semiconductors (OSCs) has drastically progressed in the recent 30 years for applications to organic field-effect transistors (OFET),[1] organic photovoltaics,[2] and organic light-emitting diodes.[3] Among them, OFETs have been investigated continuously for a long period of time.[4] From the beginning of research in OFETs, p-type OSCs have been extensively designed starting from pentacene,[5] and the mobility has been improved from an order of 10$^{-5}$ to over 10 cm$^2$ V$^{-1}$ s$^{-1}$.[6] The development of n-type and ambipolar OSCs is lagging in comparison to p-type OSCs, but the research trend has largely shifted to these OSCs, and many promising small molecules and novel polymer semiconductors have achieved electron mobilities of up to 10 cm$^2$ V$^{-1}$ s$^{-1}$.[7−12] Recently, a great number of studies have been devoted to process and interface engineering in order to improve the mobility through the device fabrication method.[13] In addition, molecular engineering has been investigated by modifying molecular structures through the substitution of functional groups and the extension of $\pi$ skeletons of promising OSCs showing high mobility.[13,14] An exploration of high mobility has been attempted regardless of the transporting carrier types.[15] One of the ways to achieve high mobility is to control the molecular packing by introducing bulky substituents. In some previous works, the introduction of bulky substituents has been found to be effective in improving the OFET properties in OSCs such as pentacene,[16,17] [1]benzothieno[3,2-*b*][1]-benzothiophene (BTBT),[18,19] naphthalenediimide (NDI),[20,21] and 5,5′-bithiazolidinylidene-2,4,2′,4′-tetrathione.[22] The bulky substituents ordinarily produce steric hindrance to destroy the intermolecular interaction, but in some cases, bulky groups realize molecular packings favorable to charge transport such as herringbone and brickwork structures.

**Received:** January 20, 2020
**Revised:** April 8, 2020
**Published:** April 8, 2020

© XXXX American Chemical Society

Scheme 1. Chemical Structures of (a) BTI, (b) TIIG, and (c) DBTII, Where R = Benzyl (Bn) and 2-Phenylethyl (EtPh)

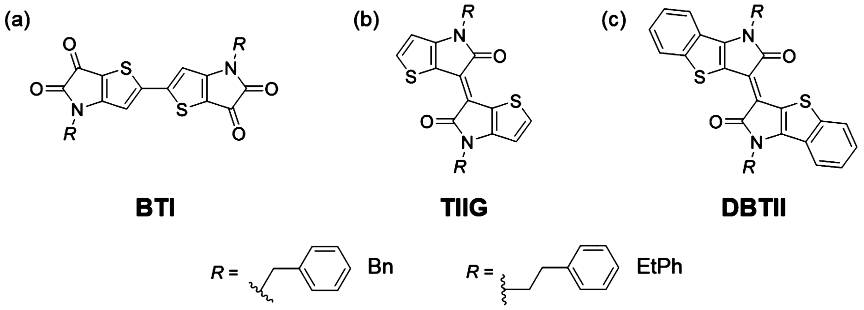

Previously, we have prepared bisthienoisatin (**BTI**; Scheme 1a) by the oxidative coupling of thienoisatins. This molecule has a linear planar structure and shows n-type OFET properties owing to the four electron-withdrawing carbonyl groups.[23] Also, we have prepared N-unsubstituted thienoisoindigo (**TIIG**; Scheme 1b) by the dimerization of thienoisatins, which has a planar molecular structure due to an intramolecular oxygen−sulfur (S···O) interaction.[24] In addition, **TIIG** forms intermolecular sulfur−sulfur (S···S) interactions and hydrogen bonds with adjacent molecules, so that this molecule shows moderate ambipolar OFET properties.[24] The derivatives with N-alkyl groups also have been investigated extensively as a repeating unit of polymers and small-molecule OSCs because the **TIIG** backbone is a promising skeleton.[25−33] Dibenzothienoisoindigo (**DBTII**; Scheme 1c), in which benzene rings are condensed with **TIIG**, is also a planar molecule and exhibits p-dominant ambipolar OFET properties on a tetratetracontane (TTC) modified substrate, showing much improved mobilities due to the extended $\pi$ skeleton.[25] However, the above three kinds of compounds have been reported only in the form with straight and branched N-alkyl chains except for N-unsubstituted **TIIG**. This has prompted us to introduce bulky phenylalkyls to **BTI**, **TIIG**, and **DBTII** cores for the purpose of investigating the effects of bulky substituents on the crystal structures and packing modes of molecules. In previous reports, a 2-phenylethyl group bearing an ethylene spacer has been effective in constructing a preferable molecular packing for carrier transport.[21,22] Thus, we have prepared *N*-2-phenylethyl (EtPh)-substituted **BTI**, **TIIG**, and **DBTII** and investigated the correlation between the crystal structures and the OFET properties. For comparison with the 2-phenylethyl-substituted molecules, *N*-benzyl (Bn)-substituted molecules have also been prepared (Scheme 1).

## EXPERIMENTAL SECTION

**Syntheses.** **BTI** was synthesized from 3-bromothiophene via introduction of phenylalkyl (**1**), cyclization to thienoisatin (**2**), and the AgF-mediated oxidative coupling of **2** with $Pd(OAc)_2$ as a catalyst (Scheme 2).[23] **TIIG** was synthesized from **2** by a homocoupling reaction using Lawesson's reagent (Scheme 2). **DBTII** was prepared by the same route as for **TIIG** from 3-bromobenzo[*b*]thiophene (Scheme 3).

**Crystal Preparation.** Single crystals of **EtPh-BTI** (260 °C), **Bn-TIIG** (230 °C), **Bn-DBTII** (320 °C), and **EtPh-DBTII** (310 °C) were obtained from sublimation under an $N_2$ atmosphere (flow rate, 50 mL/min; pressure, 10 Pa). Crystals of **Bn-BTI** were obtained from a chloroform solution, and single crystals of **EtPh-TIIG** were obtained from a toluene solution.

**X-ray Diffraction.** Single-crystal X-ray structure analyses were carried out by a Rigaku R-AXIS RAPID II imaging plate diffractometer with Cu K$\alpha$ radiation from a rotating anode source with a confocal multilayer X-ray mirror (Rigaku VM-spider, $\lambda$ = 1.54187 Å). The structures were solved by the dual-space method (SHELXT)[34] and refined by the full-matrix least-squares method by applying anisotropic temperature factors for all non-hydrogen atoms using the SHELXL programs.[35] The hydrogen atoms were placed at geometrically calculated positions. A twin analysis of **Bn-BTI** was conducted by PLATON because crystals of **Bn-BTI** have non-merohedral twins.[36]

Scheme 2. Synthetic Scheme to BTI and TIIG

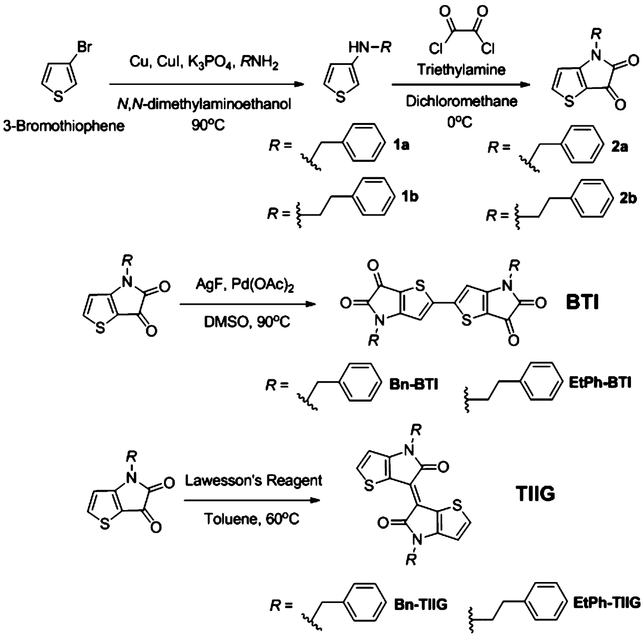

The thin-film X-ray diffraction (XRD) patterns were taken by using a Philips X'Pert-Pro-MRD instrument with Cu K$\alpha$ radiation ($\lambda$ = 1.540598 Å). Two-dimensional grazing incidence wide-angle X-ray scattering (GIWAXS) patterns were obtained at SPring-8 on beamline BL40B2.[37] The samples were irradiated at a fixed incidence angle on the order of 0.125°, and the GIWAXS patterns were recorded with a 2-D image detector (PILATUS3 S 2M). The wavelength of the X-ray beam was 1 Å (energy of 12.39 keV), and the camera length was 350.4 mm.

## RESULTS AND DISCUSSION

**Electronic Properties.** The highest occupied molecular orbital (HOMO) and lowest unoccupied molecular orbital (LUMO) levels are estimated by using cyclic voltammetry and ultraviolet visible (UV−vis) absorption spectroscopy. **Bn-BTI** and **EtPh-BTI** show two reversible reduction waves similar to those of the previous alkyl-**BTI** (Figure 1a),[23] whereas **Bn-DBTII** and **EtPh-DBTII** exhibit two reversible oxidation

**Scheme 3. Synthetic Scheme to DBTII**

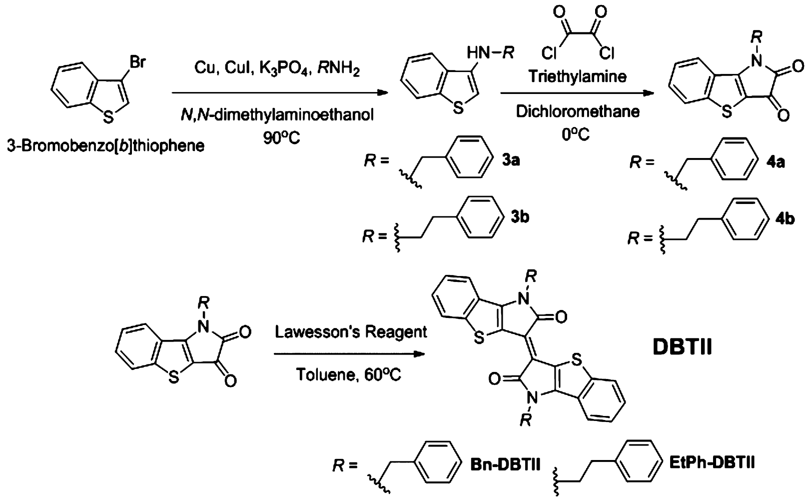

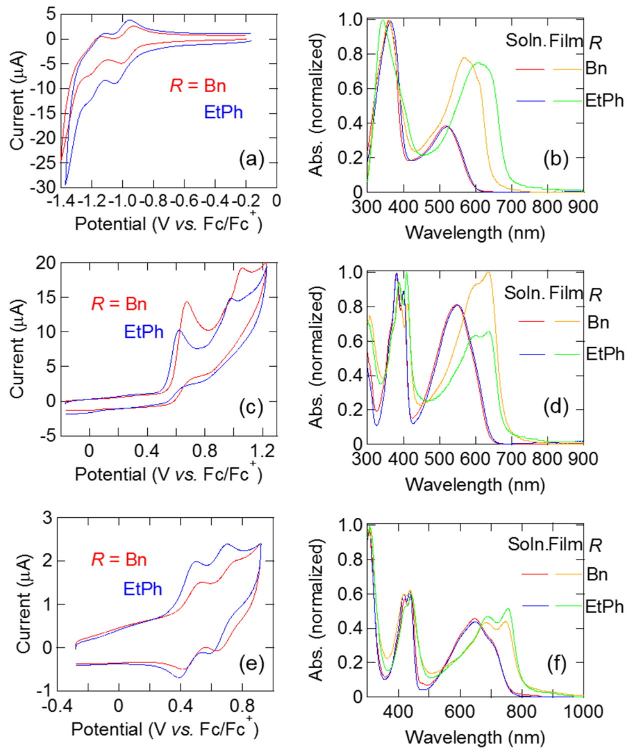

**Figure 1.** Cyclic voltammograms of (a) **BTIs**, (c) **TIIGs**, and (e) **DBTIIs**. UV–vis absorption spectra of (b) **BTIs**, (d) **TIIGs**, and (f) **DBTIIs**.

waves (Figure 1e). However, **Bn-TIIG** and **EtPh-TIIG** show two irreversible oxidation peaks (Figure 1c); thus the HOMO levels are estimated from the onset potentials ($E_{\mathrm{onset}}$). In other molecules, the HOMO or LUMO levels are estimated from the first half-wave oxidation (**DBTIIs**) or reduction (**BTIs**) potentials ($E_{1/2}$) as given in Table 1. The HOMO–LUMO gaps ($E_g^{\mathrm{opt}}$) are extracted from $\lambda_{\mathrm{onset}}$ values of the solution absorption spectra. The LUMO levels of **BTIs** are about −3.8 eV, which denotes relatively low lying LUMO levels due to the four electron-withdrawing carbonyl groups. **TIIGs** and **DBTIIs** are expected to show ambipolar OFET properties because the LUMO levels are lower than −3.15 eV and the HOMO levels are higher than −5.6 eV.[38] The absorption spectra of the thin films are red-shifted owing to the intermolecular interactions in the solid state (Figures 1b,d,f). In the thin films of **TIIGs** and **DBTIIs**, the absorption bands are almost identical regardless of the substituents (Table 2). However, the absorption band of **EtPh-BTI** is shifted to long wavelength much more than for **Bn-BTI**. This means intermolecular interactions are strong in **EtPh-BTI** in comparison with **Bn-BTI** (see Crystal Structures). Here, the excited energy levels split greatly, resulting in a narrow energy gap in the solid state.

**Table 2. Optical Properties of the Thin Films**

| compd | R | $\lambda_{\mathrm{onset}}$ (nm) | $\lambda_{\mathrm{max}}$ (nm) | $E_g^{\mathrm{opt}}$ (eV) |
|---|---|---|---|---|
| **BTI** | Bn | 646 | 359, 569 | 1.92 |
| | EtPh | 687 | 343, 607 | 1.80 |
| **TIIG** | Bn | 685 | 388, 412, 635 | 1.81 |
| | EtPh | 679 | 388, 409, 636 | 1.82 |
| **DBTII** | Bn | 798 | 306, 439, 684, 747 | 1.55 |
| | EtPh | 799 | 306, 443, 690, 754 | 1.55 |

**Table 1. Summary of Electrochemical and Optical Properties in the Solutions**

| compd | R | $E_{1/2}$ (V) | $E_{\mathrm{onset}}$ (V) | $E_{\mathrm{LUMO}}$ (eV) | $\lambda_{\mathrm{onset}}$ (nm) | $\lambda_{\mathrm{max}}$ (nm) | $E_g^{\mathrm{opt}}$ (eV) | $E_{\mathrm{HOMO}}$ (eV) |
|---|---|---|---|---|---|---|---|---|
| **BTI** | Bn | −0.97 | | −3.83 | 594 | 360, 518 | 2.09 | −5.92[a] |
| | EtPh | −1.00 | | −3.80 | 600 | 364, 521 | 2.06 | −5.86[a] |
| **TIIG** | Bn | | 0.57 | −3.43[b] | 639 | 380, 400, 548 | 1.94 | −5.37 |
| | EtPh | | 0.52 | −3.39[b] | 643 | 381, 400, 551 | 1.93 | −5.32 |
| **DBTII** | Bn | 0.48 | | −3.65[b] | 758 | 306, 421, 441, 647 | 1.63 | −5.28 |
| | EtPh | 0.44 | | −3.60[b] | 756 | 306, 418, 438, 649 | 1.64 | −5.24 |

[a] Estimated by subtracting $E_g^{\mathrm{opt}}$ from $E_{\mathrm{LUMO}}$. [b] Estimated by adding $E_g^{\mathrm{opt}}$ to $E_{\mathrm{HOMO}}$.

**Crystal Structures.** In all crystals, the molecules are centrosymmetric, and the half-molecule is crystallographically independent. **Bn-DBTII** crystallizes in a triclinic system, and the others crystallize in monoclinic systems. All molecules in the monoclinic structures form stacks in which the molecules are oppositely tilted from the molecules in the adjacent columns (**EtPh-BTI**, **Bn-TIIG**, and **EtPh-DBTII**) or from the adjacent layers (**Bn-BTI** and **EtPh-TIIG**), although all molecules are parallel in **Bn-DBTII**. In general, the molecular cores are perfectly planar, but the phenyl rings are tilted, exceeding 70° in Bn and less than 22° in EtPh (Figure 2a,e, Figure 3a,e, Figure 4a,e, and Table 7). Crystallographic data are given in Table 3.

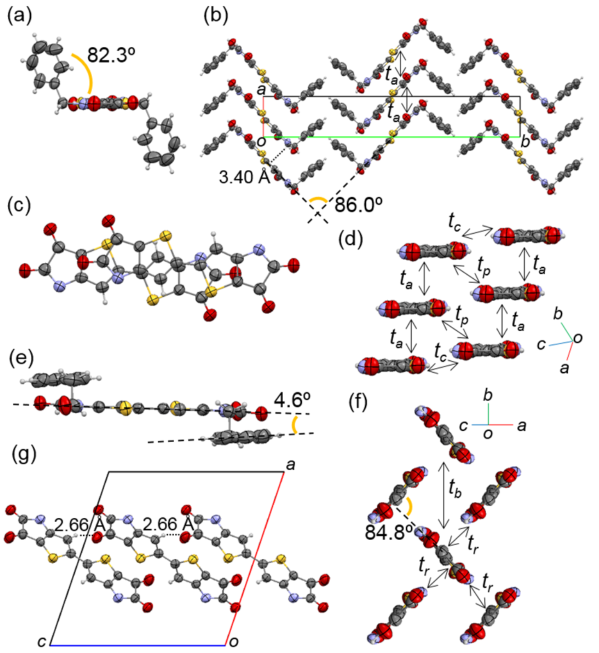

**Figure 2.** (a) Molecular structure of **Bn-BTI**. (b) Crystal structure of **Bn-BTI** viewed along the *c* axis. (c) Molecular overlap mode. (d) Crystal structure of **Bn-BTI** viewed along the long axis of the molecular core. (e) Molecular structure of **EtPh-BTI**. Crystal structure of **EtPh-BTI** viewed (f) along the long axis of the molecular core and (g) along the *b* axis. For clarity, the substituents are omitted in (c), (d), (f), and (g).

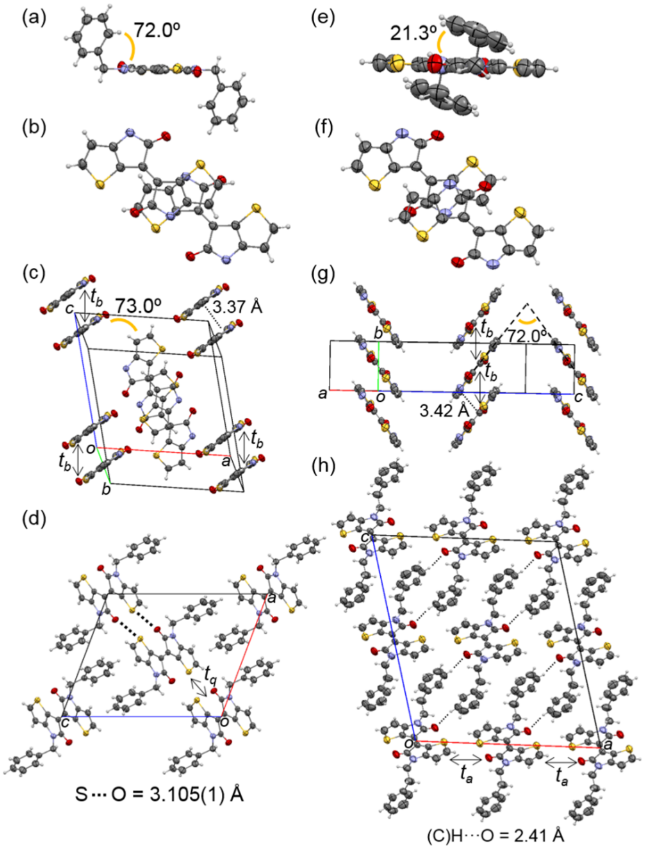

**Figure 3.** (a) Molecular structure of **Bn-TIIG** and (b) molecular overlap mode. (c) Molecular packing of **Bn-TIIG** and (d) crystal structure viewed along the *b* axis. (e) Molecular structure of **EtPh-TIIG** and (f) molecular overlap mode. Crystal structure of **EtPh-TIIG** viewed (g) along the molecular long axis and (h) along the *b* axis. For clarity, the substituents are omitted in (b), (c), (f), and (g).

**Bn-BTI** forms a uniform stacking structure along the *a* axis with an interplanar spacing of 3.40 Å (Figure 2b). The stacked molecules are slipped mainly along the long axis of the molecular core (Figure 2c). Molecules in the same *ac* layer are parallel, but molecules in the adjacent layers are alternately tilted (86.0°); these layers are stacked along the *b* axis (Figure 2b). An S···S interaction with a distance of 3.511(2) Å and an S···O intermolecular interaction with a distance of 3.263(4) Å are observed along the *c* axis (Figure S5c). Accordingly, the transfer integrals ($t_c$ and $t_p$) in the transverse direction are comparable to $t_a$ along the stacking axis (Figure 2d and Table 4); these transfer integrals suggest a comparatively isotropic conduction, though the magnitude is not large.

The crystal structure of **EtPh-BTI** looks like a herringbone structure (Figure 2f), but the molecules are largely slipped along the long axis of the molecular core (Figure 2g and Figure S6b). This structure involves side by side intermolecular interactions (Figure 2f), and hydrogen bonds with a distance of 2.66 Å are formed in C═O···H along the *c* axis (Figure 2g). These interactions are the origins of the largely red shifted solid-state absorption bands in comparison with **Bn-BTI**. The dihedral angle between the adjacent columns is nearly perpendicular (84.8°) (Figure 2f). Nonetheless, the large displacement along the long axis of the molecular core is disadvantageous to charge transport in comparison to the ideal herringbone structure,[39] because the transfer integrals are comparatively small (Table 4).

The crystal structure of **Bn-TIIG** is isostructural with N-unsubstituted **TIIG.**[24] **Bn-TIIG** forms a uniform stacking structure along the *b* axis with an interplanar spacing of 3.37 Å (Figure 3c). In **Bn-TIIG** and **EtPh-TIIG**, the molecular long axis is defined by the substituents and is parallel to the N−N direction. This is the perpendicular direction in Scheme 1b, and the intercolumnar direction corresponds to the horizontal direction in Scheme 1b (molecular short axis). In **Bn-TIIG**, molecules in the adjacent columns along the *a* + *c* axis are tilted to opposite directions (73.0°) (Figure 3c). In this direction, S···O intermolecular interactions with a distance of 3.105(1) Å are formed (Figure 3d); this is similar to the hydrogen bonds of N-unsubstituted **TIIG.**[24]

**EtPh-TIIG** forms a uniform stacking structure along the *b* axis with an interplanar spacing of 3.42 Å (Figure 3g). The adjacent columns along the *a* axis are parallel (Figure 3h), whereas the molecules in the adjacent layers are alternately tilted by about 72.0° in opposite directions; the layers are

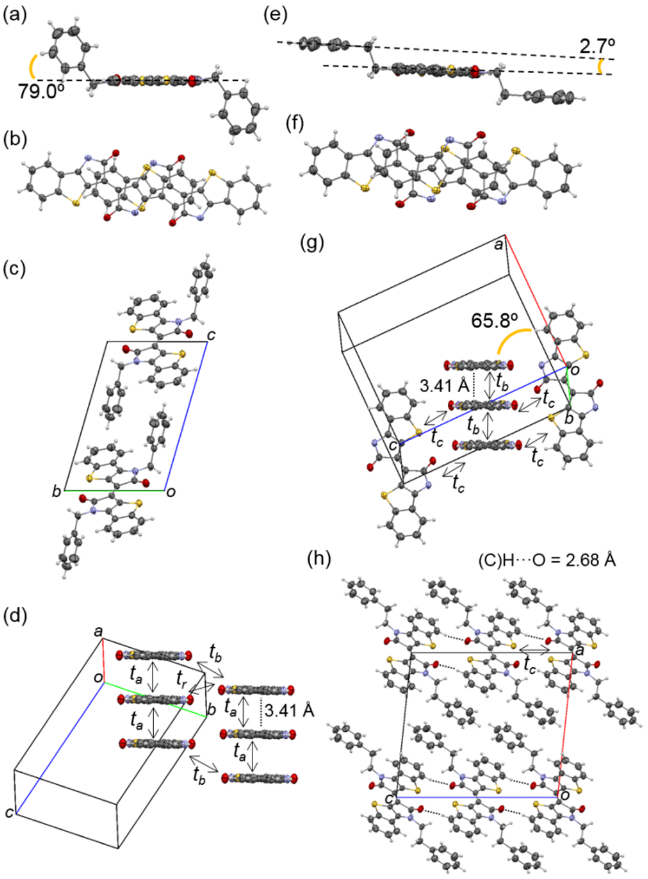

**Figure 4.** (a) Molecular structure of **Bn-DBTII** and (b) molecular overlap mode. Crystal structure of **Bn-DBTII** viewed (c) along the *a* axis and (d) along the long axis of the molecular core. (e) Molecular structure of **EtPh-DBTII** and (f) molecular overlap mode. (g) Molecular packing of **EtPh-DBTII** and (h) crystal structure viewed along the *b* axis. For clarity, the substituents are omitted in (b), (d), (f), and (g).

**Table 4. Electron Transfer Integrals (meV) of BTIs**

| R | $t_a$ | $t_b$ | $t_c$ | $t_p$ | $t_r$ |
|---|---|---|---|---|---|
| Bn | −32.9 |  | −15.3 | 21.8 |  |
| EtPh |  | 8.3 |  |  | 27.8 |

stacked along the *c* axis (Figure 3g). **EtPh-TIIG** has a large intramolecular torsion angle (21.3°) between the **TIIG** plane and the phenyl ring of **EtPh** in comparison to other **EtPh**-substituted molecules (Figure 3e). Between C=O of the molecular core and a phenyl hydrogen of **EtPh**, a hydrogen bond is formed (distance 2.41 Å) (Figure 3h); thus, this interaction indicates a relatively large intramolecular torsion angle.

In **Bn-TIIG**, the transfer integral along the stacking axis is larger for the LUMO than for the HOMO (Table 5). In contrast, **EtPh-TIIG** has a particularly large transfer integral for the HOMO. This difference comes from the slip distance along the molecular short axis, though the slip distance along the molecular long axis is the same (Figure 3b,f and Figures S7 and S8). The large displacement in **Bn-TIIG** results in a ring-overatom structure (Figure 3b), though the comparatively small displacement in **EtPh-TIIG** results in a ring-overbond structure (Figure 3f).

**Table 5. Transfer Integrals (meV) of TIIGs**

| R |  | $t_a$ | $t_b$ | $t_q$ |
|---|---|---|---|---|
| Bn | HOMO |  | −28.7 | 4.0 |
|  | LUMO |  | 42.9 | −14.3 |
| EtPh | HOMO | −3.7 | −118.1 |  |
|  | LUMO | −3.4 | 67.2 |  |

In **Bn-DBTII** and **EtPh-DBTII**, the molecular long axis is defined by the molecular core and the substituents block the molecular sides. These molecules form uniform stacking structures with interplanar spacings of 3.41 Å along the *a* and *b* axes, respectively (Figure 4). In **Bn-DBTII**, all molecules are parallel, and an intercolumnar interaction exists along the *b*

**Table 3. Crystallographic Data**

|  | Bn-BTI | EtPh-BTI | Bn-TIIG | EtPh-TIIG | Bn-DBTII | EtPh-DBTII |
|---|---|---|---|---|---|---|
| chem formula | $C_{26}H_{16}N_2O_4S_2$ | $C_{28}H_{20}N_2O_4S_2$ | $C_{26}H_{18}N_2O_2S_2$ | $C_{28}H_{22}N_2O_2S_2$ | $C_{34}H_{22}N_2O_2S_2$ | $C_{36}H_{26}N_2O_2S_2$ |
| formula wt | 484.54 | 512.60 | 454.56 | 482.61 | 554.68 | 582.73 |
| cryst syst | monoclinic | monoclinic | monoclinic | monoclinic | triclinic | monoclinic |
| space group | $P2_1/n$ | $P2_1/c$ | $P2_1/n$ | $C2/c$ | $P\bar{1}$ | $P2_1/c$ |
| *a* (Å) | 4.91789(9) | 13.6380(3) | 12.6820(3) | 19.5477(6) | 6.37399(12) | 14.2197(3) |
| *b* (Å) | 30.6056(6) | 7.18687(16) | 5.66961(13) | 5.60960(19) | 8.36881(15) | 6.28460(11) |
| *c* (Å) | 7.66360(14) | 13.0238(3) | 15.4096(4) | 22.1929(7) | 12.9434(2) | 15.7764(3) |
| *α* (deg) | 90 | 90 | 90 | 90 | 104.1072(7) | 90 |
| *β* (deg) | 100.2339(9) | 108.7680(13) | 110.6364(12) | 104.1203(17) | 98.5380(7) | 95.9370(7) |
| *γ* (deg) | 90 | 90 | 90 | 90 | 100.3249(7) | 90 |
| *V* (Å$^3$) | 1135.13(4) | 1208.65(5) | 1036.89(4) | 2360.02(13) | 645.27(2) | 1402.30(4) |
| *Z* | 2 | 2 | 2 | 4 | 1 | 2 |
| total no. of rflns | 13117 | 13557 | 11296 | 12872 | 7637 | 15470 |
| no. of unique rflns ($R_{int}$) | 2062 (0.0576) | 2214 (0.0353) | 1899 (0.0552) | 2162 (0.0328) | 2332 (0.0498) | 2575 (0.0407) |
| $D_{calcd}$ (g/cm$^3$) | 1.418 | 1.408 | 1.456 | 1.358 | 1.427 | 1.380 |
| R1[a] | 0.0671 | 0.0486 | 0.0445 | 0.0516 | 0.0476 | 0.0403 |
| wR2[b] | 0.2239 | 0.1711 | 0.1194 | 0.1767 | 0.1318 | 0.1133 |
| GOF | 1.130 | 1.140 | 1.081 | 1.124 | 1.175 | 1.153 |
| *T* (K) | 298 | 275 | 275 | 275 | 298 | 298 |

[a] $R1(F^2 > 2\sigma(F^2))$. [b] $wR2(F^2)$ for all observed reflections.

https://dx.doi.org/10.1021/acs.cgd.0c00087
Cryst. Growth Des. XXXX, XXX, XXX−XXX

axis (Figure 4c). The phenyl group of **Bn-DBTII** stretches toward the *c* axis facing the phenyl group of the next layer molecule (Figure 4c). The molecular cores construct a one-dimensional conduction path along the stacking axis because there are no obvious intercolumnar short contacts (Figure 4d). In **EtPh-DBTII**, molecules in the adjacent columns aligned along the *c* axis are alternately tilted by about 65.8° in opposite directions (Figure 4g). Along this axis, intermolecular hydrogen bonds are formed between C═O of the molecular core and the hydrogen of the condensed benzene ring (Figure 4h). The overlap modes of **Bn-DBTII** and **EtPh-DBTII** are approximately the same (Figure 4b,f). Along the short axis of the **DBTII** plane, **Bn-DBTII** is slightly slipped while **EtPh-DBTII** is not slipped (Figures S9 and S10). Consequently, as reflected in the transfer integrals, these molecules show the same tendency that overlaps in the HOMO are much larger than overlaps in the LUMO along the stacking direction (Table 6).

**Table 6. Transfer Integrals (meV) of DBTIIs**

| R | | $t_a$ | $t_b$ | $t_c$ | $t_r$ |
|---|---|---|---|---|---|
| Bn | HOMO | 57.6 | −4.3 | | −1.2 |
| | LUMO | −33.1 | −6.3 | | 1.0 |
| EtPh | HOMO | | 78.7 | −9.0 | |
| | LUMO | | −42.8 | −3.1 | |

In summary, only **EtPh-BTI** constructs a two-dimensional conduction path with a herringbone structure, while the other molecules form uniform stacking structures (Table 7). Among them, all molecules are parallel in **Bn-DBTII**, whereas the adjacent columns are alternately tilted in **Bn-TIIG** and **EtPh-DBTII**. In **Bn-BTI** and **EtPh-TIIG**, the adjacent columns are parallel but the adjacent layers are alternately tilted in the opposite directions. The phenyl rings of the benzyl and 2-phenylethyl groups are not oriented parallel to the molecular core, but the tilt angles of the phenyl rings in the 2-phenylethyl groups are considerably smaller than those in the benzyl groups because the ethylene spacer in the 2-phenylethyl group enables a more appropriate orientation of the phenyl ring (Table 7). In addition, hydrogen bonds are observed only in the 2-phenylethyl-substituted molecules. Therefore, the ethylene spacer is more effective in forming an undistorted molecular structure.

**Table 7. Summary of Torsion Angle and Short Contacts with π−π Distances**

| compd | R | between cores and phenyl rings (deg) | S···O interaction (Å) | hydrogen bond distance C═O···H (Å) | interplanar π−π distance (Å) |
|---|---|---|---|---|---|
| **BTI** | Bn | 82.3 | 3.263(4) (inter) | | 3.40 |
| | EtPh | 4.6 | | 2.66 | |
| **TIIG** | Bn | 72.0 | 3.105(1) (inter), 2.859(1) (intra) | | 3.37 |
| | EtPh | 21.3 | 2.859(2) (intra) | 2.41 | 3.42 |
| **DBTII** | Bn | 79.0 | 2.810(1) (intra) | | 3.41 |
| | EtPh | 2.7 | 2.806(1) (intra) | 2.68 | 3.41 |

Only **Bn-BTI** forms an S···S interaction, and **Bn-BTI** and **Bn-TIIG** have intermolecular S···O interactions. In **TIIG**s and **DBTII**s, intramolecular S···O interactions which guarantee the molecular core planarity are observed (Figures S7a−S10a).

**Thin-Film Properties.** By measurement of thin-film XRD and GIWAXS, molecular orientations in the thin films are investigated (Figure 5). **Bn-BTI** and EtPh-substituted molecules show sharp XRD peaks, but weak XRD peaks are observed in **Bn-TIIG** and **Bn-DBTII**. The extracted *d* values agree well with the out-of-plane peaks of GIWAXS (Table 8). In some cases, in-plane peaks are observed as well. Many sharp peaks are observed in **EtPh-TIIG** and **EtPh-DBTII**, indicating good crystallinity of these thin films.

In **Bn-BTI**, the *d* spacing is estimated to be 15.3 Å from XRD and GIWAXS ($q_z$ = 0.41 Å$^{-1}$). This value corresponds to half of the *b* axis. In addition, in the in-plane GIWAXS, $q_{xy}$ = 0.82 Å$^{-1}$ (=7.65 Å) and $q_{xy}$ = 1.30 Å$^{-1}$ (=4.82 Å) are observed, which are very close to the values for $c \sin \alpha \sin \beta$ (=7.54 Å) and $a \sin \beta \sin \gamma$ (=4.84 Å), respectively. Therefore, the crystallographic *ac* plane is aligned parallel to the substrate, where the tilt angle of the **BTI** plane from the substrate normal is 43° (Figure S12).

In **EtPh-BTI**, the *d* spacing is estimated to be 18.9 Å from XRD and GIWAXS ($q_z$ = 0.33 Å$^{-1}$). Although this value is longer than any axes of the unit cell, the length of the molecular long axis including **EtPh** is 18.6 Å and is close to the *d* spacing. In addition, in the in-plane GIWAXS, the same peak is observed at $q_{xy}$ = 0.33 Å$^{-1}$ (=18.9 Å), indicating that the molecular long axis is parallel to the substrate. Therefore, with retainment of the herringbone structure, the face-on and side-on orientations are mixed on the substrate (Figure S13). In the side-on orientation, the tilt angle of the **BTI** plane from the substrate normal is nearly 90° (84.8°). This orientation is superposed with the face-on orientation, in which the **BTI** plane is parallel to the substrate.

The XRD of **Bn-TIIG** shows two kinds of *d* spacings, 11.8 and 7.7 Å, which correspond to $q_z$ = 0.53 Å$^{-1}$ (=11.8 Å) and $q_z$ = 0.82 Å$^{-1}$ (=7.65 Å) in the out-of-plane GIWAXS. The former corresponds to the value for $a \sin \beta \sin \gamma$ (=11.87 Å), and the latter is close to half of the value for $c \sin \alpha \sin \beta$ (=7.3 Å). Therefore, two types of orientations coexist in the thin films, in which the crystallographic *bc* and *ab* planes are aligned parallel to the substrate. In the former case, the tilt angle of the **TIIG** plane is 22° from the substrate normal; this is basically the side-on orientation (Figure S14). In the latter case, the tilt angle of the **TIIG** plane is 32° from the substrate normal; this is the edge-on orientation (Figure S14). In the in-plane GIWAXS, peaks at $q_{xy}$ = 0.54 Å$^{-1}$ (=11.7 Å) and $q_{xy}$ = 0.82 Å$^{-1}$ (=7.65 Å) are observed. This observation also supports the coexistence of two kinds of orientations.

The XRD and out-of-plane GIWAXS in **EtPh-TIIG** show the same *d* spacing of 13.8 Å ($q_z$ = 0.456 Å$^{-1}$), but this value is larger than half of the *c* axis (11.1 Å). This implies that the molecules in the thin films are less tilted than the molecules in the single crystals. The thin-film tilt angle from the vertical direction to the substrate ($\beta'$) is calculated from $l = d/\cos \beta'$, where *l* is the molecule length estimated from the crystal structure (19.9 Å) and *d* is the *d* spacing (13.8 Å). This leads to $\beta'$ = 46°, which is slightly smaller than the single-crystal value of 48°. In the thin films, the molecules are oriented more

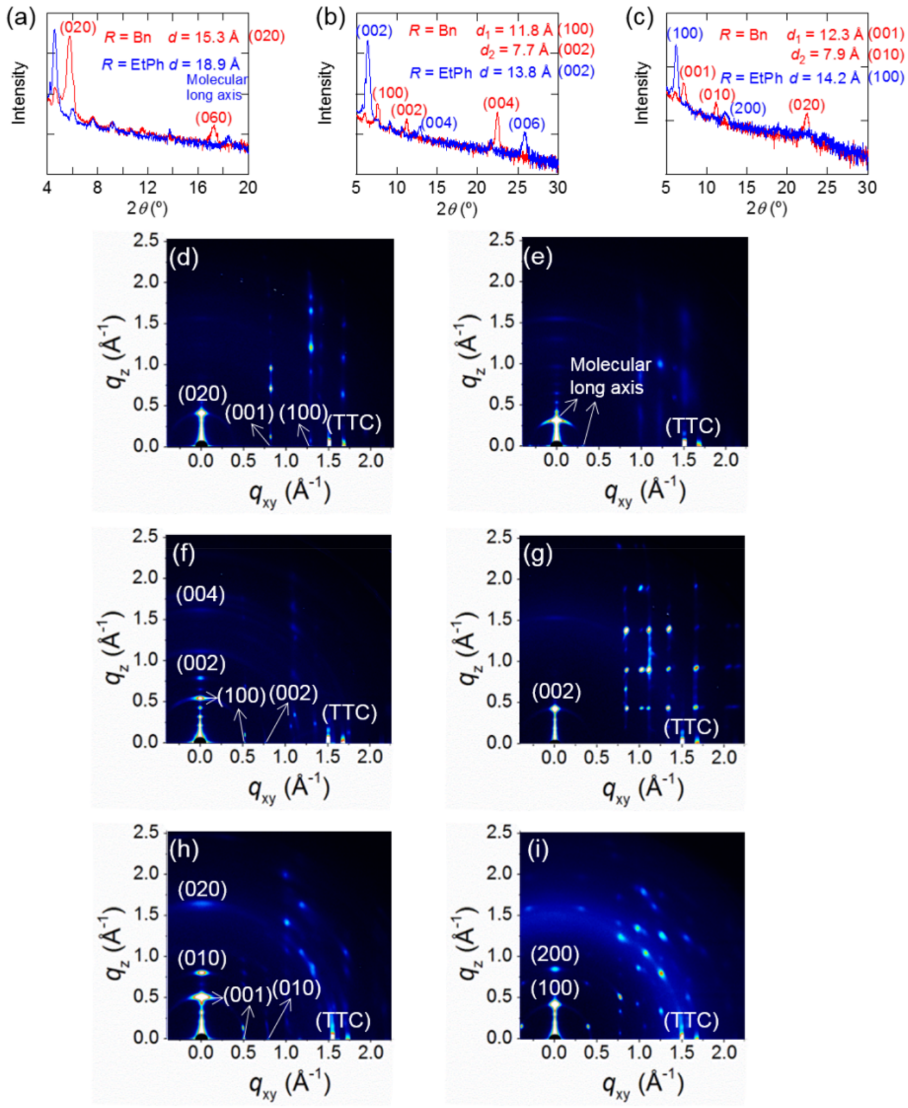

**Figure 5.** XRD patterns of (a) **BTIs**, (b) **TIIGs**, and (c) **DBTIIs**. GIWAXS patterns of (d) **Bn-BTI**, (e) **EtPh-BTI**, (f) **Bn-TIIG**, (g) **EtPh-TIIG**, (h) **Bn-DBTII**, and (i) **EtPh-DBTII**.

**Table 8. XRD and GIWAXS *d* Values (Å)**

| | | | GIWAXS (*hkl*) | |
|---|---|---|---|---|
| compd | R | XRD (*hkl*) | out of plane | in plane |
| **BTI** | Bn | 15.3 (020), 5.1 (060) | 15.3 (020) | 7.65 (001), 4.82 (100) |
| | EtPh | 18.9 (molecular long axis) | 18.9 (molecular long axis) | 18.9 (molecular long axis) |
| **TIIG** | Bn | 11.8 (100), 7.7 (002), 3.85 (004) | 11.8 (100), 7.65 (002), 3.85 (004) | 11.7 (100), 7.65 (002) |
| | EtPh | 13.8 (002), 6.9 (004), 3.45 (006) | 13.8 (002) | |
| **DBTII** | Bn | 12.3 (001), 7.9 (010), 3.95 (020) | 12.3 (001), 7.91 (010), 3.95 (020) | 12.3 (001), 7.91 (010) |
| | EtPh | 14.2 (100), 7.14 (200) | 14.2 (100), 7.13 (200) | |

closely to the perpendicular direction in comparison to the single crystals (Figure S15).

The XRD of **Bn-DBTII** shows two *d* spacings, 12.3 and 7.9 Å, which correspond to $q_z$ = 0.51 Å$^{-1}$ (=12.3 Å) and $q_z$ = 0.79 Å$^{-1}$ (=7.91 Å) in the out-of-plane GIWAXS, respectively. In the single crystal, $c \sin \alpha \sin \beta$ is 12.3 Å and $b \sin \alpha \sin \gamma$ is 7.9 Å; thus, these values are in good agreement with the values of extracted *d* spacings. In addition, in-plane GIWAXS peaks are observed at $q_{xy}$ = 0.51 Å$^{-1}$ (=12.3 Å) and $q_{xy}$ = 0.79 Å$^{-1}$ (=7.91 Å). Similarly to **Bn-TIIG**, two types of orientations coexist in the thin films; the crystallographic *ab* and *ac* planes are aligned parallel to the substrate. The tilt angle of the **DBTII** plane is 55° from the substrate normal in the edge-on orientation and 26° in the side-on orientation (Figure S16).

From the out-of-plane GIWAXS and XRD of **EtPh-DBTII**, the *d* spacing is estimated to be 14.2 Å ($q_z$ = 0.44 Å$^{-1}$). This value is close to that for $a \sin \beta \sin \gamma$ (=14.14 Å), indicating that the *bc* plane is aligned parallel to the substrate. Therefore, the molecules are arranged in an edge-on orientation, and the tilt angle of the **DBTII** plane is 47° from the substrate normal (Figure S17).

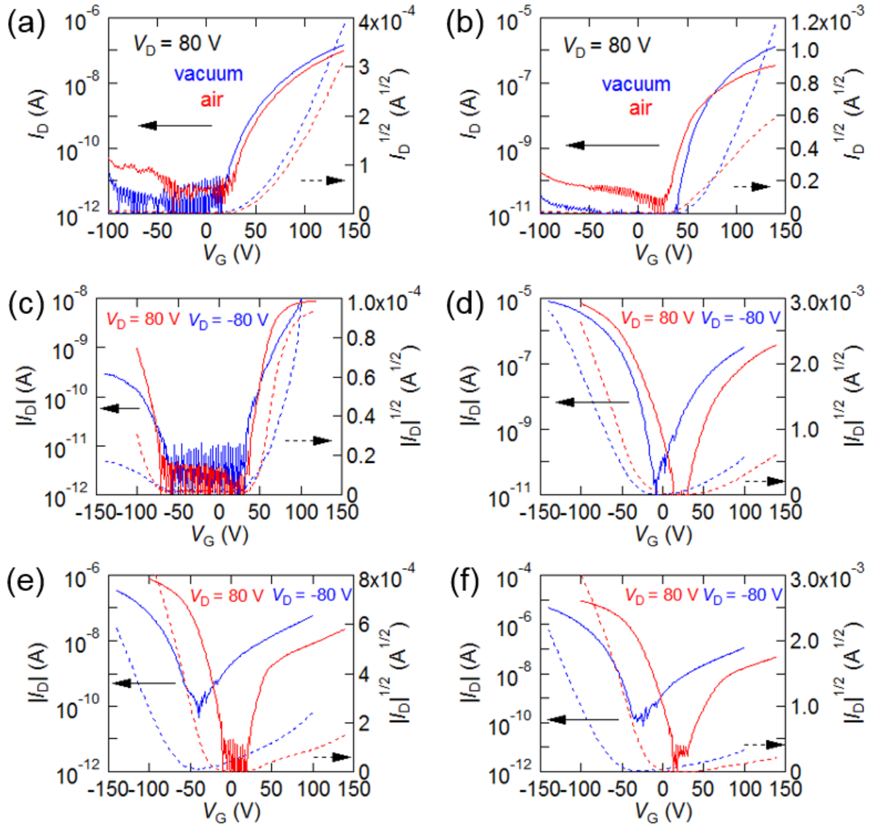

**Figure 6.** Transfer characteristics of (a) **Bn-BTI**, (b) **EtPh-BTI**, (c) **Bn-TIIG**, (d) **EtPh-TIIG**, (e) **Bn-DBTII**, and (f) **EtPh-DBTII**.

**Table 9. OFET Properties of BTIs, TIIGs, and DBTIIs**

| | | hole | | | electron | | |
|---|---|---|---|---|---|---|---|
| compd | measurement | $\mu_{av}$ [$\mu_{max}$] ($cm^2\ V^{-1}\ s^{-1}$) | $V_T$ (V) | $I_{on}/I_{off}$ | $\mu_{av}$ [$\mu_{max}$] ($cm^2\ V^{-1}\ s^{-1}$) | $V_T$ (V) | $I_{on}/I_{off}$ |
| **Bn-BTI** | under vacuum | | | | $5.4 \times 10^{-4}$ [$7.2 \times 10^{-4}$] | 60 | $10^5$ |
| | in air | | | | $2.9 \times 10^{-4}$ [$3.7 \times 10^{-4}$] | 63 | $10^4$ |
| **EtPh-BTI** | under vacuum | | | | $6.4 \times 10^{-3}$ [0.01] | 67 | $10^5$ |
| | in air | | | | $9.6 \times 10^{-4}$ [$1.8 \times 10^{-3}$] | 50 | $10^4$ |
| **Bn-TIIG** | under vacuum | $6.3 \times 10^{-7}$ [$1.2 \times 10^{-6}$] | −41 | $10^2$ | $9.4 \times 10^{-5}$ [$2.3 \times 10^{-4}$] | 44 | $10^4$ |
| **EtPh-TIIG** | under vacuum | 0.017 [0.039] | −38 | $10^5$ | $1.3 \times 10^{-3}$ [$3.5 \times 10^{-3}$] | 64 | $10^4$ |
| **Bn-DBTII** | under vacuum | $2.4 \times 10^{-3}$ [$4.7 \times 10^{-3}$] | −70 | $10^3$ | $5.3 \times 10^{-5}$ [$8.3 \times 10^{-5}$] | 35 | $10^4$ |
| **EtPh-DBTII** | under vacuum | 0.027 [0.051] | −68 | $10^5$ | $9.1 \times 10^{-5}$ [$1.7 \times 10^{-4}$] | 36 | $10^3$ |

**Transistor Properties.** **BTIs** show n-type transistor characteristics under vacuum and in air because the HOMO levels are too low to show hole transport (Table 1 and Figure 6). **EtPh-BTI** exhibits improved mobility of more than 1 order of magnitude in comparison to **Bn-BTI**. This is attributable to the tilt angles from the substrate normal in the thin films. In general, when the molecules are arranged more closely to the substrate normal, the mobility is improved.[40] Even though face-on-arranged molecules coexist in **EtPh-BTI**, the side-on-arranged molecules are oriented more perpendicularly to the substrate in comparison to **Bn-BTI**. However, the mobilities of these two molecules decrease in comparison to the previously reported alkyl-**BTIs**.[23] The reason is roughness and many grain boundaries in the thin films, as confirmed by AFM (Figure S11a,b). In **EtPh-BTI**, a two-dimensional conduction path is constructed in the herringbone structure, but one of the conduction paths faces the direction vertical to the substrate in the thin films (Figure S13). Consequently, a one-dimensional conduction path is formed between the electrodes, leading to the reduced mobility. Upon air exposure, **BTIs** show slightly decreased OFET properties and the off current increases. These phenomena are consistent with the relatively high LUMO levels in comparison with the air-stable n-type molecules, which have LUMO levels below −4.0 eV.[39] However, owing to the passivation effect of the bulky substituents,[41−44] the air stability is improved in comparison to the previously reported alkyl-**BTIs**.[23] OFET properties of **BTIs**, **TIIGs**, and **DBTIIs** are given in Table 9.

**TIIGs** and **DBTIIs** exhibit ambipolar transistor characteristics under vacuum (Figure 6). **Bn-TIIG** shows n-dominant ambipolar properties, which is consistent with the transfer integrals (Table 5). Other molecules exhibit p-dominant ambipolar properties, which are attributable to the large transfer integrals between the HOMO and the better donor abilities of those molecules as shown in the relatively high HOMO levels (−5.2 to − 5.4 eV, Table 1), which are closer to the work function of the gold electrodes.[45] Among the four molecules, the Bn-substituted molecules exhibit lower OFET properties. The Bn-substituted molecules have two kinds of orientations in the thin films, and the randomness is the origin of the ineffective carrier transport. In comparison, improved OFET properties are observed in the EtPh-substituted molecules. In particular, **EtPh-TIIG** exhibits a maximum hole mobility of about 0.04 $cm^2 V^{-1} s^{-1}$, which is higher than that of N-unsubstituted **TIIG**.[24] This comes from the considerably large transfer integral between the HOMOs of the stacking molecules. The electron mobility is comparable to that of N-unsubstituted **TIIG**. **EtPh-DBTII** shows much higher hole mobility due to the extended $\pi$ skeleton with a reduced reorganization energy for holes (Table S1). However, in comparison to hexyl-**DBTII**,[25] hole and electron mobilities are reduced because of the large tilt angle of the molecular cores from the substrate normal (47°) in the thin films (Figure S17).

## CONCLUSIONS

In this paper, we have investigated benzyl (Bn)- and 2-phenylethyl (EtPh)-substituted bisthienoisatin (**BTI**), thienoisoindigo (**TIIG**), and dibenzothienoisoindigo (**DBTII**) molecules. Since the energy levels depend only on the molecular core, these molecules show HOMO and LUMO levels similar to those of the alkyl-substituted **BTI**, **TIIG**, and **DBTII**. The HOMO levels decrease in the order **DBTII**s < **TIIG**s < **BTI**s, and the LUMO levels decrease in the order **TIIG**s < **DBTII**s < **BTI**s. Therefore, **BTI**s show n-type OFET properties and **TIIG**s and **DBTII**s exhibit ambipolar OFET properties, which are in good agreement with the expectations from the energy levels. These molecules form uniform stacking structures, though **EtPh-BTI** has a slipped herringbone structure, and a few intermolecular interactions are observed owing to the bulky substituents. The benzyl parts have large torsion angles from the molecular core, while the 2-phenylethyl parts have small torsion angles from the molecular core. This is because the latter has an ethylene spacer that is adequate to enable suitable molecular packing. Therefore, the 2-phenylethyl substitution is more advantageous to the carrier transport, and this is evident from the OFET mobilities, which are about 0.01 $cm^2 V^{-1} s^{-1}$ for electrons in **EtPh-BTI** and 0.04 and 0.05 $cm^2 V^{-1} s^{-1}$ for holes in **EtPh-TIIG** and **EtPh-DBTII**, respectively. In contrast, from the thin film XRD and GIWAXS, it is indicated that two kinds of molecular arrangements coexist in the thin films of the benzyl-substituted **TIIG** and **DBTII**. This is unfavorable for the carrier transport, which is confirmed by the OFET mobilities of **Bn-TIIG** and **Bn-DBTII**. In **TIIG**s, the dominant carrier polarity in OFET is opposite; **Bn-TIIG** shows n-dominant properties but **EtPh-TIIG** shows p-dominant properties. This is caused by the difference in slip distance along the molecular short axis, as reflected in the transfer integrals.

The present work demonstrates how benzyl and 2-phenylethyl substitutions affect the crystal structures and OFET properties in **BTI**, **TIIG**, and **DBTII**. It is confirmed that one-dimensional stacking structures are maintained in almost all cases, even though the bulky substituents are attached at the nitrogen face to the short-axis side of the molecular core. These results give us a hint for designing side substituents of small-molecule and polymer OSCs.

## ASSOCIATED CONTENT

### Supporting Information

Crystal data (CIF) The Supporting Information is available free of charge at https://pubs.acs.org/doi/10.1021/acs.cgd.0c00087.

Additional information on material synthesis, electrochemical properties, and optical properties, DFT calculations, thermal properties, crystal structures, thin-film microstructures and morphologies, and thin-film transistor properties (PDF)

### Accession Codes

CCDC 1974945–1974950 contain the supplementary crystallographic data for this paper. These data can be obtained free of charge via www.ccdc.cam.ac.uk/data_request/cif, or by emailing data_request@ccdc.cam.ac.uk, or by contacting The Cambridge Crystallographic Data Centre, 12 Union Road, Cambridge CB2 1EZ, UK; fax: +44 1223 336033.

## AUTHOR INFORMATION

### Corresponding Authors

**Dongho Yoo** − *Department of Materials Science and Engineering, Tokyo Institute of Technology, Tokyo 152-8552, Japan;* orcid.org/0000-0003-0886-7533; Email: dongho312@postech.ac.kr

**Minoru Ashizawa** − *Department of Materials Science and Engineering, Tokyo Institute of Technology, Tokyo 152-8552, Japan;* orcid.org/0000-0002-6810-256X; Email: ashizawa.m.aa@m.titech.ac.jp

**Takehiko Mori** − *Department of Materials Science and Engineering, Tokyo Institute of Technology, Tokyo 152-8552, Japan;* orcid.org/0000-0002-0578-5885; Email: mori.t.ae@m.titech.ac.jp

### Authors

**Akihiro Kohara** − *Department of Materials Science and Engineering, Tokyo Institute of Technology, Tokyo 152-8552, Japan*

**Tadashi Kawamoto** − *Department of Materials Science and Engineering, Tokyo Institute of Technology, Tokyo 152-8552, Japan;* orcid.org/0000-0002-5676-4013

**Hiroyasu Masunaga** − *Japan Synchrotron Radiation Research Institute (JASRI/SPring-8), Hyogo 679-5198, Japan*

**Noboru Ohta** − *Japan Synchrotron Radiation Research Institute (JASRI/SPring-8), Hyogo 679-5198, Japan*

**Hidetoshi Matsumoto** − *Department of Materials Science and Engineering, Tokyo Institute of Technology, Tokyo 152-8552, Japan;* orcid.org/0000-0002-4949-1184

Complete contact information is available at: https://pubs.acs.org/10.1021/acs.cgd.0c00087

### Notes

The authors declare no competing financial interest.

## ACKNOWLEDGMENTS

The authors are grateful to the Center for Advanced Materials Analysis, Tokyo Institute of Technology, for X-ray diffraction measurements. The authors also thank Professor Hidehiro Uekusa for use of the Rigaku VM-spider. GIWAXS experiments were performed on beamline BL40B2 at SPring-8 with the approval of the Japan Synchrotron Radiation Research Institute (JASRI) (Proposal No. 2019B1006). This work was partially supported by JPSJ KAKENHI Grant Number

18H02044 and the Takahashi Industrial and Economic Research Foundation.

## REFERENCES

(1) Bao, Z.; Locklin, J. *Organic Field-Effect Transistors*, 1st ed.; CRC Press: Boca Raton, FL, 2007.

(2) Sun, S.-S.; Sariciftci, N. S. *Organic photovoltaics: mechanism, materials, and devices*, CRC Press: Boca Raton, FL, 2005.

(3) Müllen, K.; Scherf, U. *Organic light-emitting devices: synthesis, properties and applications*; Wiley-VCH: Weinheim, Germany, 2006.

(4) Mori, T. Molecular Materials for Organic Field-Effect Transistors. *J. Phys.: Condens. Matter* **2008**, *20*, 184010.

(5) Kudo, K.; Yamashina, M.; Moriizumi, T. Field Effect Measurement of Organic Dye Films. *Jpn. J. Appl. Phys.* **1984**, *23*, 130−130.

(6) Mori, T. Organic Charge-Transfer Salts and the Component Molecules in Organic Transistors. *Chem. Lett.* **2011**, *40*, 428−434.

(7) Meng, Q.; Hu, W. Recent Progress of N-Type Organic Semiconducting Small Molecules for Organic Field-Effect Transistors. *Phys. Chem. Chem. Phys.* **2012**, *14*, 14152−14164.

(8) Zhao, Y.; Guo, Y.; Liu, Y. 25th Anniversary Article: Recent Advances in n-Type and Ambipolar Organic Field-Effect Transistors. *Adv. Mater.* **2013**, *25*, 5372−5391.

(9) Quinn, J. T. E.; Zhu, J.; Li, X.; Wang, J.; Li, Y. Recent Progress in the Development of N-Type Organic Semiconductors for Organic Field Effect Transistors. *J. Mater. Chem. C* **2017**, *5*, 8654−8681.

(10) Zhou, K.; Dong, H.; Zhang, H.; Hu, W. High Performance N-Type and Ambipolar Small Organic Semiconductors for Organic Thin Film Transistors. *Phys. Chem. Chem. Phys.* **2014**, *16*, 22448−22457.

(11) Xu, X.; Yao, Y.; Shan, B.; Gu, X.; Liu, D.; Liu, J.; Xu, J.; Zhao, N.; Hu, W.; Miao, Q. Electron Mobility Exceeding 10 $cm^2 V^{-1} s^{-1}$ and Band-Like Charge Transport in Solution-Processed n-Channel Organic Thin-Film Transistors. *Adv. Mater.* **2016**, *28*, 5276−5283.

(12) Xue, G.; Wu, J.; Fan, C.; Liu, S.; Huang, Z.; Liu, Y.; Shan, B.; Xin, H. L.; Miao, Q.; Chen, H.; Li, H. Boosting the Electron Mobility of Solution-Grown Organic Single Crystals *via* Reducing the Amount of Polar Solvent Residues. *Mater. Horiz.* **2016**, *3*, 119−123.

(13) Dong, H.; Fu, X.; Liu, J.; Wang, Z.; Hu, W. 25th Anniversary Article: Key Points for High-Mobility Organic Field-Effect Transistors. *Adv. Mater.* **2013**, *25*, 6158−6183.

(14) Okamoto, T. Next-Generation Organic Semiconductors Driven by Bent-Shaped $\pi$-Electron Cores. *Polym. J.* **2019**, *51*, 825−833.

(15) Paterson, A. F.; Singh, S.; Fallon, K. J.; Hodsden, T.; Han, Y.; Schroeder, B. C.; Bronstein, H.; Heeney, M.; McCulloch, I.; Anthopoulos, T. D. Recent Progress in High-Mobility Organic Transistors: A Reality Check. *Adv. Mater.* **2018**, *30*, 1801079.

(16) Anthony, J. E. Functionalized Acenes and Heteroacenes for Organic Electronics. *Chem. Rev.* **2006**, *106*, 5028−5048.

(17) Park, S. K.; Jackson, T. N.; Anthony, J. E.; Mourey, D. A. High Mobility Solution Processed 6,13-Bis(Triisopropyl-Silylethynyl) Pentacene Organic Thin Film Transistors. *Appl. Phys. Lett.* **2007**, *91*, 063514.

(18) Iino, H.; Usui, T.; Hanna, J. Liquid Crystals for Organic Thin-Film Transistors. *Nat. Commun.* **2015**, *6*, 6828.

(19) Usta, H.; Kim, D.; Ozdemir, R.; Zorlu, Y.; Kim, S.; Ruiz Delgado, M. C.; Harbuzaru, A.; Kim, S.; Demirel, G.; Hong, J.; Ha, Y.-G.; Cho, K.; Facchetti, A.; Kim, M.-G. High Electron Mobility in [1]Benzothieno[3,2- *b* ][1]Benzothiophene-Based Field-Effect Transistors: Toward n-Type BTBTs. *Chem. Mater.* **2019**, *31*, 5254−5263.

(20) Jung, B. J.; Sun, J.; Lee, T.; Sarjeant, A.; Katz, H. E. Low-Temperature-Processible, Transparent, and Air-Operable n-Channel Fluorinated Phenylethylated Naphthalenetetracarboxylic Diimide Semiconductors Applied to Flexible Transistors. *Chem. Mater.* **2009**, *21*, 94−101.

(21) Song, I.; Lee, S.-C.; Shang, X.; Ahn, J.; Jung, H.-J.; Jeong, C.-U.; Kim, S.-W.; Yoon, W.; Yun, H.; Kwon, O.-P.; Oh, J. High-Performance Visible-Blind UV Phototransistors Based on n-Type Naphthalene Diimide Nanomaterials. *ACS Appl. Mater. Interfaces* **2018**, *10*, 11826−11836.

(22) Iijima, K.; Le Gal, Y.; Lorcy, D.; Mori, T. Impact of Bulky Phenylalkyl Substituents on the Air-Stable n-Channel Transistors of Birhodanine Analogues. *RSC Adv.* **2018**, *8*, 18400−18405.

(23) Yoo, D.; Luo, X.; Hasegawa, T.; Ashizawa, M.; Kawamoto, T.; Masunaga, H.; Ohta, N.; Matsumoto, H.; Mei, J.; Mori, T. n-Type Organic Field-Effect Transistors Based on Bisthienoisatin Derivatives. *ACS Appl. Electron. Mater.* **2019**, *1*, 764−771.

(24) Yoo, D.; Hasegawa, T.; Ashizawa, M.; Kawamoto, T.; Masunaga, H.; Hikima, T.; Matsumoto, H.; Mori, T. N-Unsubstituted Thienoisoindigos: Preparation, Molecular Packing and Ambipolar Organic Field-Effect Transistors. *J. Mater. Chem. C* **2017**, *5*, 2509−2512.

(25) Hasegawa, T.; Ashizawa, M.; Matsumoto, H. Design and Structure−Property Relationship of Benzothienoisoindigo in Organic Field Effect Transistors. *RSC Adv.* **2015**, *5*, 61035−61043.

(26) Dasari, R. R.; Dindar, A.; Lo, C. K.; Wang, C.-Y.; Quinton, C.; Singh, S.; Barlow, S.; Fuentes-Hernandez, C.; Reynolds, J. R.; Kippelen, B.; Marder, S. R. Tetracyano Isoindigo Small Molecules and Their Use in N-Channel Organic Field-Effect Transistors. *Phys. Chem. Chem. Phys.* **2014**, *16*, 19345−19350.

(27) Meager, I.; Nikolka, M.; Schroeder, B. C.; Nielsen, C. B.; Planells, M.; Bronstein, H.; Rumer, J. W.; James, D. I.; Ashraf, R. S.; Sadhanala, A.; Hayoz, P.; Flores, J.-C.; Sirringhaus, H.; McCulloch, I. Thieno[3,2-b]Thiophene Flanked Isoindigo Polymers for High Performance Ambipolar OFET Applications. *Adv. Funct. Mater.* **2014**, *24*, 7109−7115.

(28) Kim, G.; Kang, S.-J.; Dutta, G. K.; Han, Y.-K.; Shin, T. J.; Noh, Y.-Y.; Yang, C. A Thienoisoindigo-Naphthalene Polymer with Ultrahigh Mobility of 14.4 $Cm^2/V{\cdot}s$ That Substantially Exceeds Benchmark Values for Amorphous Silicon Semiconductors. *J. Am. Chem. Soc.* **2014**, *136*, 9477−9483.

(29) Lu, C.; Chen, H.-C.; Chuang, W.-T.; Hsu, Y.-H.; Chen, W.-C.; Chou, P.-T. Interplay of Molecular Orientation, Film Formation, and Optoelectronic Properties on Isoindigo- and Thienoisoindigo-Based Copolymers for Organic Field Effect Transistor and Organic Photovoltaic Applications. *Chem. Mater.* **2015**, *27*, 6837−6847.

(30) Nketia-Yawson, B.; Kang, H.; Shin, E. Y.; Xu, Y.; Yang, C.; Noh, Y. Y. Effect of Electron-Donating Unit on Crystallinity and Charge Transport in Organic Field-Effect Transistors with Thienoisoindigo-Based Small Molecules. *Org. Electron.* **2015**, *26*, 151−157.

(31) Onwubiko, A.; Yue, W.; Jellett, C.; Xiao, M.; Chen, H.-Y.; Ravva, M. K.; Hanifi, D. A.; Knall, A.-C.; Purushothaman, B.; Nikolka, M.; Flores, J.-C.; Salleo, A.; Bredas, J.-L.; Sirringhaus, H.; Hayoz, P.; McCulloch, I. Fused Electron Deficient Semiconducting Polymers for Air Stable Electron Transport. *Nat. Commun.* **2018**, *9*, 416.

(32) Song, E.; Ha, Y. H.; Kang, B.; Yun, H.-J.; Kwon, S.-K.; Kim, Y.-H.; Cho, K. Effects of Varying the Lengths of the Donor Units in $\pi$-Extended Thienothiophene Isoindigo-Based Polymer Semiconductors. *J. Mater. Chem. C* **2018**, *6*, 9972−9980.

(33) Raj, M. R.; Kim, Y.; Park, C. E.; An, T. K.; Park, T. Effect of the Length of a Symmetric Branched Side Chain on Charge Transport in Thienoisoindigo-Based Polymer Field-Effect Transistors. *Org. Electron.* **2019**, *65*, 251−258.

(34) Sheldrick, G. M. *SHELXT* − Integrated Space-Group and Crystal-Structure Determination. *Acta Crystallogr., Sect. A: Found. Adv.* **2015**, *71*, 3−8.

(35) Sheldrick, G. M. Crystal Structure Refinement with *SHELXL*. *Acta Crystallogr., Sect. C: Struct. Chem.* **2015**, *71*, 3−8.

(36) Spek, A. L. *CheckCIF* Validation ALERTS: What They Mean and How to Respond. *Acta Crystallogr. Sect. E Crystallogr. Commun.* **2020**, *76*, 1−11.

(37) Fujisawa, T.; Inoue, K.; Oka, T.; Iwamoto, H.; Uruga, T.; Kumasaka, T.; Inoko, Y.; Yagi, N.; Yamamoto, M.; Ueki, T. Small-Angle X-Ray Scattering Station at the SPring-8 RIKEN Beamline. *J. Appl. Crystallogr.* **2000**, *33*, 797−800.

(38) Tang, M. L.; Reichardt, A. D.; Wei, P.; Bao, Z. Correlating Carrier Type with Frontier Molecular Orbital Energy Levels in Organic Thin Film Transistors of Functionalized Acene Derivatives. *J. Am. Chem. Soc.* **2009**, *131*, 5264−5273.

(39) Iijima, K.; Le Gal, Y.; Higashino, T.; Lorcy, D.; Mori, T. Birhodanines and Their Sulfur Analogues for Air-Stable n-Channel Organic Transistors. *J. Mater. Chem. C* **2017**, *5*, 9121−9127.

(40) Kakinuma, T.; Kojima, H.; Ashizawa, M.; Matsumoto, H.; Mori, T. Correlation of Mobility and Molecular Packing in Organic Transistors Based on Cycloalkyl Naphthalene Diimides. *J. Mater. Chem. C* **2013**, *1*, 5395−5401.

(41) Kanno, M.; Bando, Y.; Shirahata, T.; Inoue, J.; Wada, H.; Mori, T. Stabilization of Organic Field-Effect Transistors in Hexamethylenetetrathiafulvalene Derivatives Substituted by Bulky Alkyl Groups. *J. Mater. Chem.* **2009**, *19*, 6548−6555.

(42) Nagakubo, J.; Ashizawa, M.; Kawamoto, T.; Tanioka, A.; Mori, T. Stabilization of Organic Field-Effect Transistors by Tert-Butyl Groups in Dibenzotetrathiafulvalene Derivatives. *Phys. Chem. Chem. Phys.* **2011**, *13*, 14370−14377.

(43) Kurosawa, T.; Chiu, Y.-C.; Zhou, Y.; Gu, X.; Chen, W.-C.; Bao, Z. Impact of Polystyrene Oligomer Side Chains on Naphthalene Diimide-Bithiophene Polymers as n-Type Semiconductors for Organic Field-Effect Transistors. *Adv. Funct. Mater.* **2016**, *26*, 1261−1270.

(44) Minemawari, H.; Tanaka, M.; Tsuzuki, S.; Inoue, S.; Yamada, T.; Kumai, R.; Shimoi, Y.; Hasegawa, T. Enhanced Layered-Herringbone Packing Due to Long Alkyl Chain Substitution in Solution-Processable Organic Semiconductors. *Chem. Mater.* **2017**, *29*, 1245−1254.

(45) Yasuda, T.; Goto, T.; Fujita, K.; Tsutsui, T. Ambipolar Pentacene Field-Effect Transistors with Calcium Source-Drain Electrodes. *Appl. Phys. Lett.* **2004**, *85*, 2098−2100.